



## A Study of the Taylor-Couette Flow with Finned Surface Rotation

M. Carlos Álvarez<sup>1†</sup>, W. Vicente<sup>1</sup>, F. Solorio<sup>1</sup>, E. Mancilla<sup>2</sup>, M. Salinas<sup>1</sup> and V. R. Zenit<sup>2</sup>

<sup>1</sup> *Institute of Engineering, UNAM, Coyoacan 04510, Mexico City, Mexico*

<sup>2</sup> *Institute of Materials Research, UNAM, Coyoacan 04510, Mexico City, Mexico*

†Corresponding Author Email: [malvarezs@iingen.unam.mx](mailto:malvarezs@iingen.unam.mx)

(Received August 29, 2018; accepted December 11, 2018)

### ABSTRACT

In this study, the Taylor-Couette flow was disturbed by incorporating annular fins over the inner rotating surface. The finned surface had three parameters: height, width, and length between fins. In this work, seven different fin configurations, in which only the fin height varied, were examined and compared using experimental and numerical techniques. We found that annular fins disturbed the flow behavior by reducing the smooth critical Taylor number ( $Ta=57.18$ ), but more important, we noticed a vortex enlargement induced by the incorporation of a relatively modest perturbation ( $b<0.5$ ) and this change remained in a wider range ( $0.57<T<14.18$ ). On the other hand, it was identified the appearance of smaller secondary vortices just over the fins, it is as a result of an increment in fin height. The relevance of this finding lies on the field of micro-mixing processes.

**Keywords:** Critical rotation rate; Taylor vortex; Annular fins; Taylor-couette flow; Finned rotor; CFD; Vorticity; Micromixing.

### 1. INTRODUCTION

The Taylor-Couette flow is an annular flow between two concentric cylinders, where one or both of them are rotating. This simple flow between cylinders develops on different patterns and structures when geometrical and rotating conditions are varied. Geoffrey Ingram Taylor (1923) found that certain flow instabilities occur when a critical rotation rate is reached; this flow instability consists of toroidal structures, and the particular pattern appears along the cylinders uniformly. Nowadays, these structures are known as Taylor vortices, and over the years, this flow has been subject to many studies that have tested this flow pattern under different modifications.

Many authors have modified the classic Taylor-Couette flow, for example, by introducing a magnetic field numerically using a ferrofluid as the working fluid (Singh and Bajaj, 2005; Rüdiger *et al.*, 2010 and Laguerre *et al.*, 2008). Furthermore, others have worked with different fluid conditions; Peng and Zhu (2010) studied the Taylor-Couette flow by using two immiscible fluids with different densities and viscosities, which were also separated by an interface with an insoluble surfactant. Moreover, a perfect monatomic gas and

compressible effects were considered by Manela and Frankel (2007). These kinds of studies have enlarged the knowledge on fluid dynamics in order to understand the flow behavior, but recently, it has been found that the Taylor-Couette system has great relevance in chemical applications, specifically on micro-mixing. Ogihara and Nomura (2002) produced monodispersed alumina particles in a Taylor-Couette system by hydrolyzing aluminum alkoxide in a mixture of octanol and acetonitrile, they proposed the use of each vortex as a batch reaction vessel. Sang-Hyuk *et al.* (2009) located different azimuthal slits on the inner surface of the outer cylinder in a Taylor-Couette system and it was seen that the slits did not affect the laminar transition process, but the turbulent Taylor vortex's appearance was accelerated.

Koschmieder (1975) was one of the first to study a disturbed Taylor-Couette flow by modifying the shape of the rotor. He identified changes on the vortex's wavelengths when O-rings were introduced in regular intervals on the inner cylinder. These changes and flow behavior were examined using a visualization that seeded aluminum powder on the working fluid; in the Koschmieder's work, the O-rings and the rotor were two independent solid bodies, and this fact could not ensure the flow axis

symmetry. Over the years, several studies of disturbed Taylor-Couette flow have been performed by modifying the rotor surface (Ikeda and Maxworthy, 1994; Sprague *et al.*, 2008; Sprague and Weidman, 2009; Deng *et al.*, 2010; Mahlout *et al.*, 2015; Liu *et al.*, 2011; Jeng, Tzeng and Lin, 2006; Richter *et al.*, 2008 and Pawar and Thorat, 2012), but a parametric study of the defined shape of the perturbations has not been conducted.

The introduction of slits or fins over the cylinder surfaces is a great innovation that is directly applicable to the control of chemical processes, such as mixing. In order to increase mixing efficiency, Richter *et al.* (2009) disturbed the Taylor-Couette flow by modifying the rotor surface introducing annular fins to investigate the mixing of a saponification of ethylacetate. They found that the mixing processes were optimized by these perturbations, but the changes on the flow were not described; moreover, just one finned-system configuration was tested and compared to a smooth rotor. Richter *et al.* (2008) demonstrated that annular fins increase the efficiency of the mixing process, but the effect of annular fins on the flow behavior remains unclear. Annular fins innovation has relevant application on chemical field as separation and mixing processes; therefore, factors such as reaction rate, residence times, mixing efficiency, and flow rate can be controlled by the introduction of annular fins. Due to the above, the first aim of this work is to describe the behavior of this disturbed flow and in this way emphasize its relevance into chemical field and other fields as rotor-dynamics.

The purpose of the current research is to study how the introduction of annular fins disturbs the Newtonian Taylor flow and to describe the changes caused by the rotor's surface modification. For this reason, the present work studies different finned rotor configurations to investigate the importance of the fin's parameters; mainly, this first work focused on the effect of the fin height parameter, but other approaches are examined. The description of the changes generated by the introduction of annular fins is identified in two experimental techniques: Kalliroscope visualization (KV) and particle image velocimetry (PIV). Additionally, numerical simulations are used to examine the fin height effect in a wider sense.

## 2. MATERIALS AND METHODS

### 2.1 Experimental Setup

The experimental device used in this work consists of a single stationary outer and different rotating inner cylinders. The outer cylinder had an inner diameter of 5.025 cm ( $2R_o$ ), while the inner cylinder diameter was 3.025 cm ( $2R_i$ ); both have a total height ( $L$ ) of 20 cm. As a result, the maximum gap ( $d$ ) of the system, the radius ratio ( $\eta=R_i/R_o$ ), and the aspect ratio ( $\phi=L/d$ ) were  $d=1.0$  cm,  $\eta=0.6$ , and  $\phi=20$ , respectively. This experiment was also defined by four geometrical parameters, as shown in Fig. 1. These parameters are length between fins

( $a$ ), fin height ( $b$ ), fin width ( $c$ ), and the maximum gap between cylinders ( $d$ ).

A polished glass outer cylinder was employed to enable the visualization, and the different finned rotors were manufactured in aluminum. Additionally, a square box was used for PIV measurements to reduce the distortion effects of refraction that can occur because of the curvature of the glass cylinder (Abcha *et al.*, 2008).

The finned rotors and its fins belong to the same aluminum piece, guaranteeing an axisymmetric system, unlike the O-rings used by Koschmieder (1975).

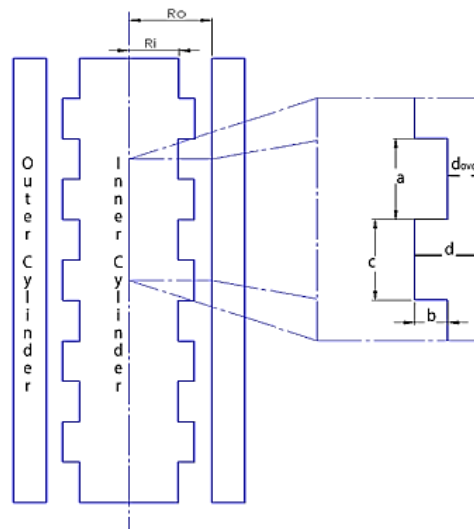


**Fig. 1. Experimental setup. Outer cylinder radius ( $R_o$ ), inner cylinder radius ( $R_i$ ), fin width ( $a$ ), height fin ( $b$ ), and length between fins ( $c$ ).**

To define the finned surface geometry, dimensionless fin parameters were used, as follows:

$$a' = \frac{a}{d}; b' = \frac{b}{d}; c' = \frac{c}{d} \quad (1)$$

where  $d = d_{over} + b$  ( $d_{over}$  is the gap between the upper surface of the fin and outer cylinder, as shown in Fig. 1).

The current work was limited to study the fin height ( $b'$ ) in a range of 0.0–0.85, while the other parameters remained constant ( $a'=1.5$  and  $c'=1.5$ ). Thus, seven finned cases were studied using numerical simulations, and three of those cases were also experimentally studied, as can be seen in Table 1.

The rotation rate of the finned rotor was controlled using a servomotor (7000 RPM, 1.21 Nm), and a mechanic coupling was used to transmit the rotation to the inner cylinder.

The flow was characterized by using the Taylor number for the smooth case (Childs, 2011), as follows:

$$Ta = \frac{\Omega_m^{0.5} d^{1.5}}{\nu} \quad (2)$$

**Table 1 Studied cases by Kalliroscope visualization (KV), particle image velocimetry (PIV), and numerical simulation (NS). Experimental cases: Smooth case, Case 2, Case 4, and Case 6.  $a'$  and  $c' = 1.5$  (for all the cases)**

Case	$b'$	Technique Employed
Smooth	0	KV, PIV and NS
Case 1	0.125	NS
Case 2	0.25	KV, PIV and NS
Case 3	0.375	NS
Case 4	0.5	KV, PIV and NS
Case 5	0.625	NS
Case 6	0.750	KV, PIV and NS
Case 7	0.875	NS

where  $r_m = \frac{R_o+R_i}{2}$  is the mean radius,  $\Omega$  is the rotation rate, and  $\nu = 9.06 \times 10^{-6} \frac{m^2}{s}$  is the kinematic viscosity of the fluid. The working fluid was glycerol and water (50 vt%) with a density ( $\rho$ ) of 960 kg/m<sup>3</sup>.

In 1963, Wallowit *et al.*, reported a critical Taylor number which has a difference of 1.85% compared with that found in this current study ( $Ta=57.18$ ). As a first hypothesis, due to the annular introduction, it was expected that the aforementioned value would be reduced while the fin height would be increased and this statement was proved by the techniques used in this work.

To identify the flow behavior changes, the present study was based on the employment of two experimental techniques and one numerical method to reproduce the phenomenon. A brief description of these techniques is presented below.

### 2.1.1 Kalliroscope Flow Visualization

The Kalliroscope flow visualization technique is based on the seeding of reflecting particles in a Newtonian fluid (Matisse and Gorman, 1984), where shearing stresses provoke the particles to align themselves, and this alignment reflects light in different intensities, allowing for a pattern flow visualization to be seen by naked eye. With this technique, the bounds of the critical rotation rate in which the Taylor vortex pattern appears for each case, were easily observed.

In the current study, a Newtonian fluid was contained in the annular gap between cylinders; the working fluid was mixed with microscopic crystals (1.2 g/L) and with methylene blue to improve contrast. The Kalliroscope fluid technique was performed in the cases proposed to delimit the critical points where the Taylor vortex pattern appeared. For this reason, the rotation rate was controlled from the rest, and it was increased with a constant acceleration ( $2.7 \times 10^{-5} \text{ rev/s}^2$ ,  $0 < Ta < 95.62$ ) while searching for the critical one. To achieve this aim, it was important to maintain the same brightness in the laboratory conditions for the analysis of each studied case. Once identified the point of the vortex appearance, the

analysis was made into a short range ( $\pm 2$  rpm) to determine the critical point. The searching of this critical value was obtained by sudden and punctual velocity testing. Additionally, the lack of hysteresis on the flow was determined using this procedure.

During these processes, photographs were taken with a digital camera (16.2 Mp.) at a rate of 10 photos/min. The experimental configurations were examined by searching for the appearance of vortices. The appearance of these vortices was determined by using image analysis software, which looked for a point in which the division of the vortex pattern appeared on each configuration with a same level of brightness. The same procedure was applied to all the photos taken from the different cases.

The second aim of the application of this technique was to identify the qualitative differences of the finned Taylor-Couette flow pattern as the geometrical fin parameters were being changed. The visualization provided by this technique allowed for the detection of the flow changes, which were mainly in the wavelength, size, and vortex position.

### 2.1.2 Particle Image Velocimetry Technique

The two-dimensional (2D) velocity fields were determined by means of the PIV technique, which was carried out using a pulsed laser light and a Phantom camera with a 35 mm lens. The experiment was aligned on the r-z plane, and the PIV results were obtained in the middle zone of the system, as illustrated in Fig. 2.

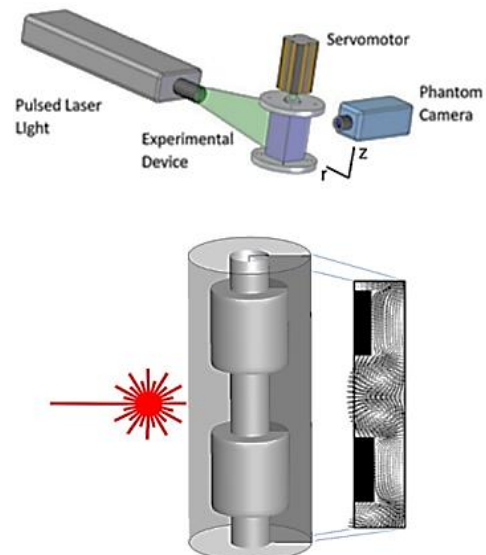


**Fig. 2. Experimental setup.**

The use of the PIV technique provided a quantitative flow description for the smooth and finned cases and gave us a better understanding of the flow behavior. In this technique, the working fluid was seeded with silver-coated hollow glass

spheres that had a mean diameter of 10 μm, a density of 1050 kg/m<sup>3</sup> and a concentration of 0.02 g/L. Dynamic processing software was used to control the system and process the acquired images. The time between image pairs varied from 200 μs to 800 μs, depending on the angular velocity of the inner cylinder. As a result, 1500 image acquisitions with a 32x32 pixels interrogation zone were taken for each experiment.

## 2.2 Numerical Method

We also conducted a computational fluid dynamics simulation of the three-dimensional (3D) Taylor-Couette flow with annular fins; it was conducted using the finite volume method. The Taylor-Couette flow was described by incompressible Newtonian and 3D Navier-Stokes equations (White, 1999), given by the following:

$$\frac{1}{r} \frac{\partial(nu_r)}{\partial r} + \frac{1}{r} \frac{\partial(u_\theta)}{\partial \theta} + \frac{\partial(u_z)}{\partial z} = 0 \quad (3)$$

$$\frac{\partial u_r}{\partial t} + (U \cdot \nabla)u_r - \frac{1}{r}u_\theta^2 = -\frac{1}{\rho} \frac{\partial P}{\partial r} + \nu \left[ \nabla^2 u_r - \frac{u_r}{r^2} - \frac{2}{r^2} \frac{\partial u_\theta}{\partial \theta} \right] \quad (4)$$

$$\frac{\partial v_\theta}{\partial t} + (U \cdot \nabla)u_\theta + \frac{1}{r}u_r u_\theta = -\frac{1}{\rho r} \frac{\partial P}{\partial \theta} + \nu \left[ \nabla^2 u_\theta - \frac{u_\theta}{r^2} + \frac{2}{r^2} \frac{\partial v_r}{\partial \theta} \right] \quad (5)$$

$$\frac{\partial u_z}{\partial t} + (U \cdot \nabla)u_z = -\frac{1}{\rho} \frac{\partial P}{\partial z} + \nu \nabla^2 u_z \quad (6)$$

where  $u_r$ ,  $u_\theta$ , and  $u_z$  are the velocity components in the radial, angular, and azimuthal direction, respectively. Moreover  $\rho$  is the density,  $P$  the pressure, and  $\nu$  the kinematic viscosity.

The unfinned and seven-finned cases were investigated by numerical simulations using the same properties of the working fluid and flow conditions reported previously in the experimental description. The annular cavity between cylinders was simulated in cylindrical coordinates ( $r$ ,  $\theta$ ,  $z$ ) where the inner cylinder was rotating at a constant rotation rate ( $\Omega$ ) and the outer one was fixed. Then, the boundary conditions to simulate the flow (non-slip condition over the outer cylinder and a constant rotation rate over the inner cylinder) were given by the following:

$$r = R_o \quad \rightarrow \quad \vec{V} = 0 \quad (7)$$

$$r = R_i \quad \rightarrow \quad u_\theta = Ri \Omega \quad (8)$$

$$r = R_i + b \quad \rightarrow \quad u_\theta = (Ri + b) \Omega \quad (9)$$

$$z = 0, L \quad \rightarrow \quad \vec{V} = 0 \quad (10)$$

In addition, the static end plates in the system were represented numerically by a non-slip condition (Eq. 10). The governing equations were solved by

using the finite-volume method, and the SIMPLE algorithm was employed for solving the pressure-velocity coupling (Patankar, 1980).

The system to be simulated had a total length ( $L$ ) of 20 a. In order to select the appropriate mesh, the angular velocity component was monitored in the middle of the gap and along the azimuthal direction. In Fig. 5, a mesh with 2,160,000 cells shows the 10 expected pairs of vortices.

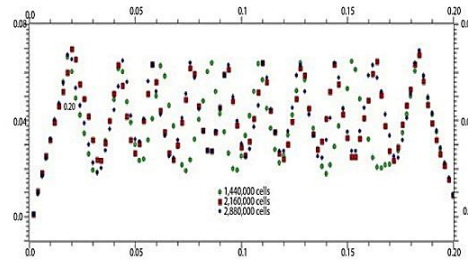


Fig. 3. Mesh independency study.

### 2.2.1 Numerical Validation

The unfinned and finned cases were simulated under the same experimental conditions,  $Ta=1.42Ta_c$ , where  $Ta_c$  is the critical Taylor number in which the Taylor vortex pattern was presented on the classic smooth case. The experimental and numerical results of case 4 are compared in Fig. 4. Both profiles (experimental and numerical) showed the same behavior (radial velocity profile, Fig. 4(a)), and the radial velocity profile presented lower differences than 3%. This profile was monitored between fins and at the middle of the gap (Fig. 4(b)).

In addition, the 3D results allowed us to observe two characteristic movements of the Taylor vortex flow, as shown in Fig. 5-I; first, the vortex rotation is represented by the vector field on a radial-azimuthal plane. Second, the vortex spinning is illustrated by streamlines around the smooth inner cylinder. In Fig. 5-II, the whole finned system is shown.

The 3D numerical results were obtained in the study, and with these results, the axisymmetric Taylor-Couette flow was verified. However, the 2D numerical results are presented to maintain consistency with the results provided by the PIV.

## 3. RESULTS AND DISCUSSION

With the aim of having a completed description of the effect of annular fins in a cylindrical flow, the present work examined the disturbed Taylor-Couette flow by using experimental and numerical techniques; all the results agreed and identified the flow changes regarding mainly on size, shape, and position of the vortex.

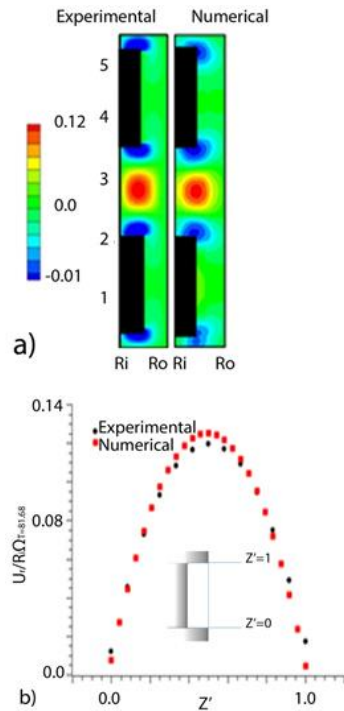


**Fig. 4. Validation of the radial velocity profile, a) Case 4 ( $b'=0.5$ ),  $Ta=81.68$  and b) inward magnitude flow between fins.**

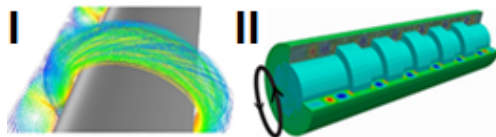


**Fig. 5. Velocity profile. I) Smooth and II) finned case.  $T=1.42$ .**

For the first effort to understand the disturbed Taylor-Couette flow, the present work examined the cylindrical system under different rotating rates using Kalliroscope visualization. The visualization outcome of the Kalliroscope technique for the smooth case at different conditions is presented in Fig. 6; for the lower rotation rates (Fig. 6-I), no brightness change along the system was observed, and this plain and laminar behavior remained unchanged within a Taylor range of  $0 < Ta < 57.18$ . On the other hand, a well-known Taylor vortex pattern was identified when a critical condition ( $Ta_c=57.18$ ) was reached (Fig. 6-II); here, the visual effect and the changes of the brightness intensity allowed us to identify the formation of each pair of vortices along the system. As was mentioned earlier, a division lines between the pair of vortices can be observed because of the use of the rheoscopic fluid.

These division lines only appear in the zone where a vortex pair is tangent and negative over the radial direction. The results show a vortex pattern composed of 10 pairs of undisturbed vortices.

In addition, the same number of undisturbed vortices of the unfinned case was verified by the numerical results. It was expected that due to the

geometrical parameter of the experimental setup, 10 pairs of undisturbed vortices would appear along the cylindrical system, which was verified; this is shown by 3D numerical simulations in Fig. 6-III.

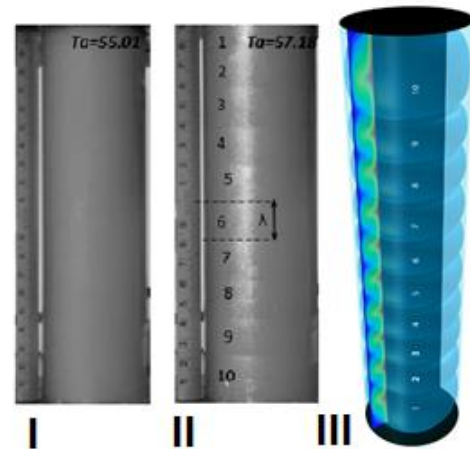


**Fig. 6. KV results: (I) Smooth classic case on Couette flow, (II) Smooth case on Taylor vortex pattern (dimensions in centimeters). (III) 3D Numerical simulations on Taylor vortex pattern.**

Complementing and supporting the vortex number, a direct measurement of the wavelength was taken ( $\lambda_s \approx 0.02$  m), which is in agreement with the next expression for the wavelength, Childs (2011):

$$\lambda_s = 2(d) \quad (11)$$

$$\lambda_s = 2(0.01)m = 0.02m$$

where  $\lambda_s$  is the predicted unfinned wavelength, and a dimensionless wavelength is defined by the following:

$$\lambda' = \frac{\lambda}{\lambda_s} \quad (12)$$

Additionally, the visualization technique allowed us to observe changes in the critical Taylor numbers when a finned system was introduced. In other words, the introduction of the fin perturbation increased the rotating flow tendency, which will be discussed later.

To examine the effect of a fin height increment over the vortex pattern and to identify the changes in flow behavior, three different configurations were experimentally tested, and the results for the studied cases are shown in Table 2 (where a relative Taylor number is defined by  $T=Ta/Ta_c$ ).

These results show an important reduction of the critical Taylor number because of the fin height increment. In the same way, different vortex sizes were identified for each of the finned tested configurations.

Furthermore, the Kalliroscope technique provided a useful description of the flow behavior and allowed us to observe the differences between the smooth and finned case patterns. The changes provoked by

the introduction of annular fins were mainly on size, shape, and position of the vortices. Figure 7 shows the qualitative changes for each of the studied cases ( $0 \leq b' \leq 0.75$ ) caused by the fin innovation over the same super critical condition ( $T=1.42$ ). The proposed finned configurations had different flow behaviors; for example, for  $b' < 0.5$ , the wavelength size increased over the undisturbed vortex wavelength ( $\lambda' > 1$ ). In contrast, the opposite effect was found when the fin height was increased ( $b' \geq 0.5$ ), showing a reduction in the vortex's wavelength ( $\lambda' < 1$ ) but an increment on vortex number.

**Table 2 Critical Taylor number ( $c'=1.5$  and  $d'=1.5$ )**

Case	$b'$	$T=T_a/T_{ac}$	$\lambda'$
Smooth	0	1	1
2	0.25	0.57	1.5
4	0.5	0.34	0.5
6	0.75	0.14	0.5 and 0.25

Another finding that came from introducing bigger fins ( $b' > 0.5$ ) was the breakdown of the vortex and a successive development of smaller vortices over the fins; this development is shown in Fig. 7 (case 6), where the pattern presents two different wavelengths ( $\lambda_1'=0.5$  and  $\lambda_2'=0.25$ , Table 2).

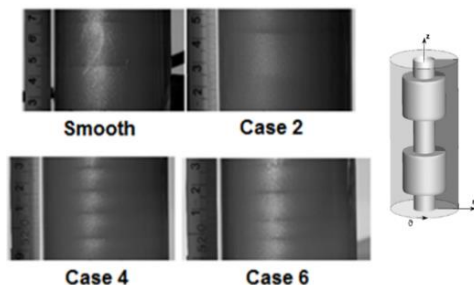


**Fig. 7. Effect of the fin height over the flow at  $T=1.42$  (wavelengths' values shown in Table 2). KV results.**

For all the experiments, the results were obtained using the same rotating condition. The associated rotation rate  $\Omega_{T=1.42}$  to the Taylor value of  $T=1.42$  was chosen because it ensured that the pattern was fully developed for the studied cases. This flow condition was used for the other techniques (2D PIV and 3D CFD simulations) to provide a direct comparison and these results are shown below.

To clarify and extend the wavelength changes due to an increase in fin height, PIV measurements were taken on the central system zone for each of the studied cases to obtain a better description of the flow behavior between two fins.

As shown in Fig. 8, the patterns of the Taylor

vortices changed in shape and position due to the increase of fin height ( $b'$ ). The vector field (Fig. 8-high) and streamlines (Fig. 8-low) show how the vortex shape was gradually deformed as the fin height varied. In contrast to what was reported by Deng *et al.* (2010), for the lower values of fin height no squared vortex deformation was identified. Case 2 showed the greatest shape deformation, and compared to the classical and regular square shape, case 2's wavelength size increased by 50% and extended over the fins. This vortex size increment has extreme importance in chemical processes, as was mentioned earlier. This increment is only present for the lower values of fin height ( $b' < 0.5$ ), however, this vortex size can be increased even more by modifying the missing fin parameters ( $a'$  and  $c'$ ), as will be discussed in a future work.

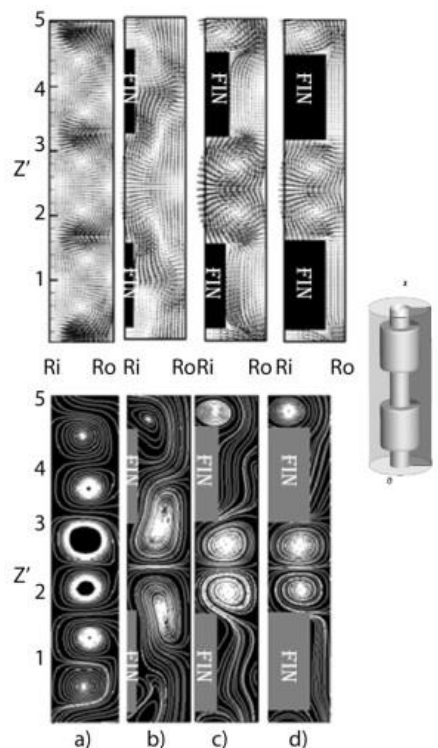


**Fig. 8. Vortex pattern: vectors (high) and streamlines (low). a) Smooth case, b) case 2, c) case 4, and d) case 6.  $T=1.42$ . PIV results.**

Additionally, it was found that for the higher values of fin height ( $b' \geq 0.5$ ), the vortices tended to be confined by the fins and the vortex shape became square again (case 4 and case 6) due to an increment on the lateral fin wall's surface and its relevance on the rotating flow tendency.

The PIV instrumentation's limitations and the presence of different flow modes and vortex rotation rates did not allow us to obtain the flow behavior information over the fins using this technique, but this information was obtained by using numerical simulation. The numerical simulation examined the fin height effect over the vortex flow in a wider way amplifying the analyzed

cases; Fig. 9 presents the flow behavior by streamlines for the finned cases and also includes the unfinned case (Table 1). These results show the deformation evolution due to the increment of the fin height, corroborating with the flow changes aforementioned through the PIV description and Kalliroscope flow visualization. Furthermore, the formation of smaller secondary vortices was detected when there was greater fin perturbation ( $b \geq 0.5$ ).

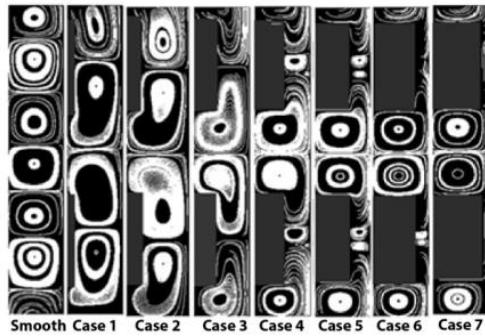


**Fig. 9. Evolution of the vortex deformation (streamlines) for the geometric characteristics shown in Table 1.  $T=1.42$ . Numerical results.**

Moreover, the PIV experimental measurements of the radial velocity profiles were taken at the central zone of the cylindrical system (Fig. 10). Here, an alternating positive and negative profile along the azimuthal direction was observed. This profile indicates a clockwise and counterclockwise rotation, which is a distinctive property of the Taylor vortex pattern. Previously, it was seen that vortices tended to be confined between the fins, but the PIV results showed a progressive increment in the radial velocity magnitude over the same area (between fins) while the fin height parameter increased; this increment over the rotatory intensity can be attributed to the presence of the longer lateral walls of the fins. The introduction of fin perturbation generated changes in several ways, including the radial velocity magnitude which was greatly affected. This magnitude had an increment of 50% when  $b'$  increased from 0.25 to 0.5 (case 2 to case 4). The radial magnitude's increment raised the rotating intensity, but more important, it caused the breakdown of the main and greater vortices, as discussed below.

Furthermore, the introduction of the annular fins affected the radial velocity component in different ways. First, the positions of negative (inward flow) and positive radial velocity zones (outward flow) were altered and could be controlled by this fin innovation. Contrary to what was reported by Deng *et al.* (2010), the inward flow was induced between fins while the outward flow was placed over the fins; this was confirmed by the three techniques employed in the present work. Comparing the radial velocity profile of the unfinned case with that of case 2, the positive zones presented a reduction over the same analyzed zone (three zones for smooth and two zones for case 2). In addition, a 14% reduction

of the maximum value of the radial velocity was found when a smaller perturbation (Case 2) was introduced.

On the other hand, the annular fin introduction induced a negative radial flow (inward flow) precisely at the middle of the zone between the fins. In other words, the vortex's position depends on the fin's axial placement. However, a higher outward flow intensity was induced near the lateral fin walls while the studied fin parameter ( $b'$ ) increased ( $b' \geq 0.5$ , case 4 and case 6). The magnitude of inward flow for case 6 increased by 134% compared to the smooth case. This difference indicates that the vortices gained rotating intensity because of the annular innovation and the increment of fin height. In this way, the rotating intensity can be controlled by the increment in fin height; this implementation could be employed in special chemical flow processes.

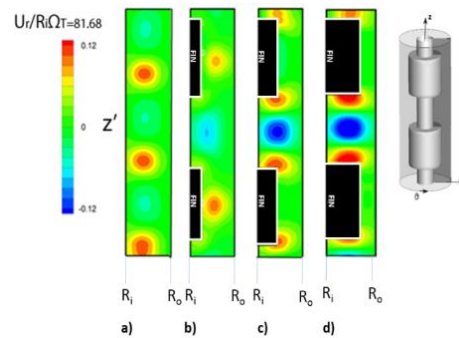


**Fig. 10. Radial velocity profile: a) Smooth case ( $b'=0$ ), b) case 2 ( $b'=0.25$ ), c) case 4 ( $b'=0.5$ ), and d) case 6 ( $b'=0.75$ ).  $T=1.42$ . PIV results.**

Additionally, the numerical results (Fig. 11(a)) show velocity differences over and below the fins due to the variations in the radius. These differences produced a pressure gradient ( $\nabla P' = 101.69$ , where  $P' = P / \frac{1}{2} \rho (R_i \Omega T_{Ta=81.68})^2$ ) that induced the negative radial flow between the fins and established the vortex's rotation (Fig. 11(b)).

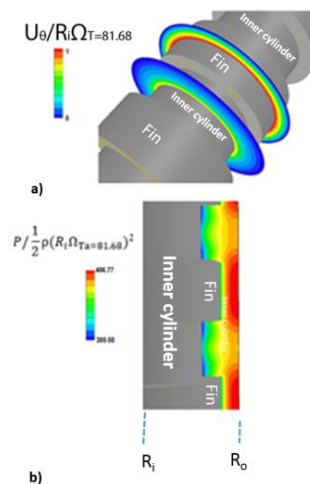


**Fig. 11. Angular velocity (a) and pressure gradient (b),  $T=1.42$ , case 4. Numerical results.**

Moreover, the numerical results were used to complement the description of the finned Taylor-Couette flow, providing the third velocity component (Fig. 12-high): angular, which was missed because of using the 2D PIV measurement.

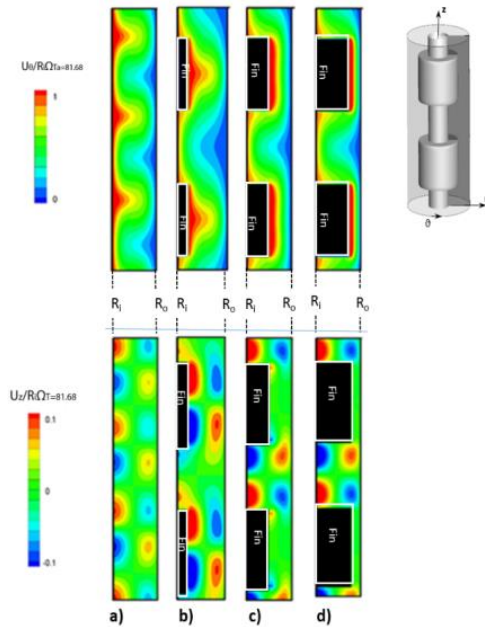


**Fig. 12. Angular velocity (high) and axial velocity (low). a) Smooth case, b) case 2, c) case 4, and d) case 6.  $T=1.42$ . Numerical results.**

The axial profile velocity is shown in Fig. 12-low. In this velocity component profile, two alternating columns along the axial direction were identified. These alternating areas represent the upward and downward flow zones, where axial movement prevails over the fins for  $b' < 0.5$  while for other cases ( $b' \geq 0.5$ , case 4 and case 6), the alternating behavior is present between the fins. More interesting is the angular velocity profile, which cannot be acquired using 2D PIV measurements (Fig. 12-high); here, a high amount of wavy behavior is found over the inner cylinder's surface, particularly for the unfinned case and case 2. The wavy behavior is the response to the centrifugal force generated by the rotor; it identifies the zone where the flow direction begins to be outward and where a pair of vortices are tangent. Once a small perturbation is introduced ( $b' < 0.5$ ), this wavy behavior comes exactly in the middle of the fins; however, for the greater perturbations ( $b' \geq 0.5$ ), this wavy behavior lessens. On the other hand, a similar wavy behavior was found on the static outer cylinder surface for all the studied cases. This behavior is a response to the flow interaction with the no-slip condition imposed over this surface and the induced spinning flow.

Additionally, some vortex identification parameters were computed to continue amplifying the flow behavior description. Although, there is no definition for a vortex, the presence of a vortex implies a region of space where the vorticity is

strong (Chong, 1990); therefore, the vorticity magnitude can be used to identify the extension of the vortices and the relative magnitude of the rotating vortex's intensity. In Fig. 13-high, we computed the vorticity magnitude to show how the vortex extension varies for the studied cases. The vorticity magnitude results, support the hypothesis that the introduction of the small annular fins increased the vortex size for case 2.

Additionally, the curvature magnitude (Braun *et al.*, 2006), as shown in Fig. 13-low, which is very large for spinning center zones, was computed to locate the vortex's centers. The vortex center tended to be between the fins, especially when the fin height increased.

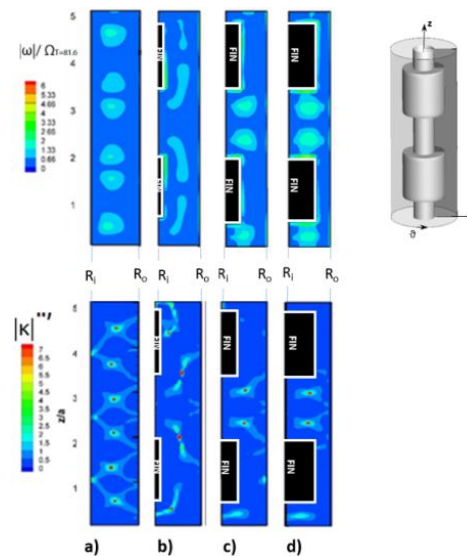


**Fig. 13. Vorticity magnitude profile (high) and curvature magnitude profile (low). a) Smooth case ( $b'=0$ ), b) case 2 ( $b'=0.25$ ), c) case 4 ( $b'=0.5$ ), and d) case 6 ( $b'=0.75$ ).  $T=1.42$ . Numerical results.**

In Fig. 14(a), the maximum point of vorticity magnitude was computed for the vicinity of the vortex centers. The minimum value of the maximum vorticity magnitude is presented in the results of case 2, which is attributed to the vortex extension and volume increment. Although a decrease was found for the vorticity magnitude, the radial flow rate, which moves from the outer to the inner cylinder (Fig. 14(b)), rose as the fin height increased, as was previously identified by the radial velocity profile.

The deployment of an annular fin into chemical reactors can enhance the mixing and separation centrifugal processes, and this must be tested on real reactors which require a high control of the rate of chemical reaction and place a vortex sub-reactor. Each vortex formation can be employed as a sub-reactor in the same Taylor-Couette system as was mentioned by Ogihara and Nomura (2002). In this work, it was demonstrated that a small fin perturbation ( $b' < 0.5$ ) created a size vortex increment and vortex deformation. However, larger

fin perturbations ( $b' \leq 0.5$ ) reduced this vortex size, but more important, we found the presence of smaller vortices over the fin due to the breakdown in the vortex.

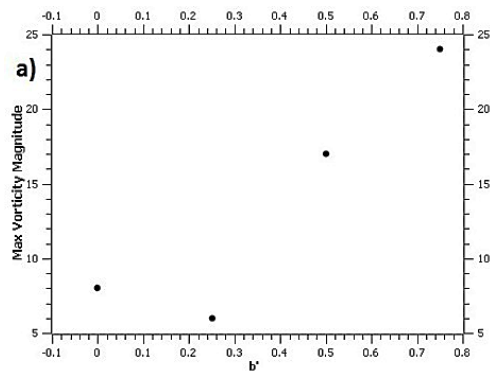


**Fig. 14. a) Max points of the vorticity magnitude and b) radial flow rate.  $T=1.42$ . Numerical results.**

To describe the formation of different size vortices in the same system and find its dependence in terms of the rotation rate, case 4 was tested using a wider range, here focusing on the flow over the fins and on the vortex breakdown. Different flow behaviors were identified over the fins, and it was found that the appearance of a different number of vortices because of the vortex breakdown and the higher rotating rates. Two vortex breakdowns were identified when the rotating condition increased within the proposed rotating range (Fig. 15). For a rotating condition of  $1.42 \leq T \leq 2.85$ , a vortex pair appeared over the fins, but if the rotating rate increased ( $T=5.71$ ), a second breakdown took place, and the two vortex pairs appeared over the same zone. According to the dimensions of this analyzed zone ( $a/d_{over}=3$ ), there would be three expected vortices over the fins. However, due to the nature of this particular flow, two vortex pairs with different sizes appeared over the fins.

Figure 16 shows the vortex breakdown evolution by monitoring radial velocity exactly over the analyzed zone (over fins). The vortex breakdown will evolve until it has a perfect symmetry for the highest rotating rate ( $T=5.71$ ). It was found that the number of secondary vortices that appeared over the fins depends on the rotating conditions and the relationship between the gap over the fins and the fins' width ( $a$ ). A large increase in the centrifugal forces (high radial velocity magnitude) is required to isolate the secondary vortices over the fins and develop them.

The introduction of annular fins, but more specifically the presence of lateral walls on higher fins, increased the centrifugal force. This force induced an outward flow and increased the radial velocity magnitude near the walls. Figure 17 shows the radial velocity profile along the total system, which consists of five annular fins. The fins are described by constant lines ( $U_r=0$ ) while two max values points are placed beside them; the inward

flow was induced between the fins, as shown previously.

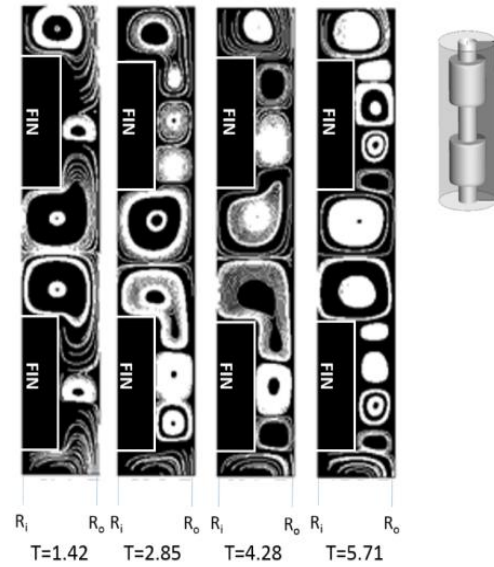


**Fig. 15. Taylor number variation to case 4 ( $b'=0.5$ ). Streamlines,  $1.42 \leq T \leq 5.71$ . Numerical results.**

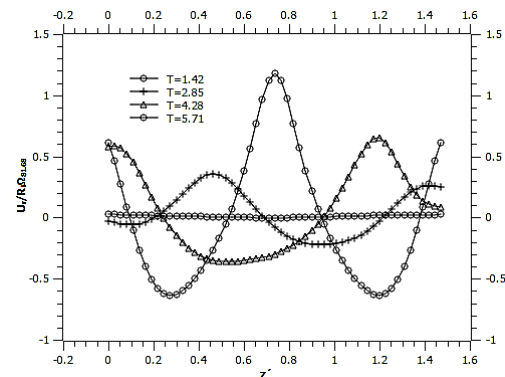


**Fig. 16. Vortex breakdown evolution for case 4,  $1.42 \leq T \leq 5.71$ . Numerical simulations.**

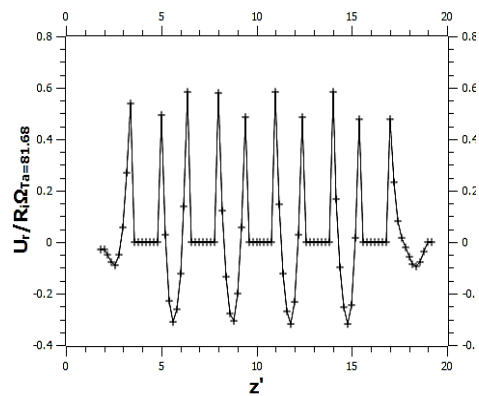


**Fig. 17. Radial velocity profile along the whole system for case 4,  $T=5.71$ .**

Contrary to the higher fin height perturbation, no changes in the vortex pattern were detected for the lower perturbation ( $b' < 0.5$ ). Even when case 2 was tested on a wider rotation rate range, no vortex breakdown was identified, but the vorticity increased (Fig. 18).

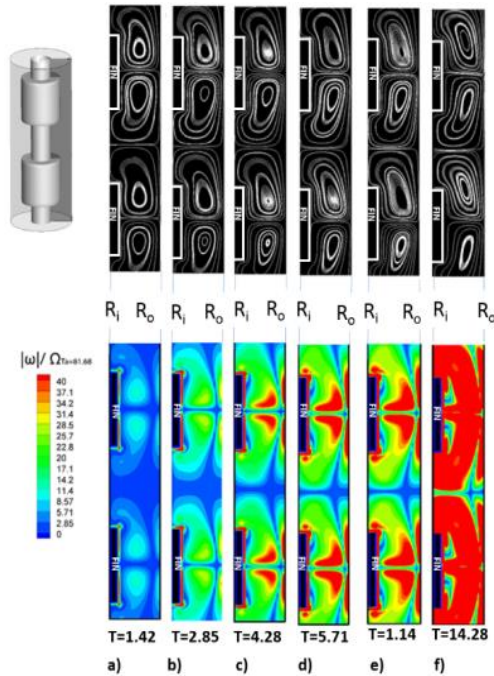


**Fig. 18. Case 2,  $1.42 \leq T \leq 14.28$ . a) Stream lines and b) vorticity magnitude. Numerical results.**

It was noted that an increment in the centrifugal force changed the flow pattern, causing a vortex breakdown ( $b' \geq 0.5$ ), and the evolution of secondary vortices changed the placement of the higher vorticity zones.

The vorticity influence between the two analyzed zones (lateral and over the fins) changed when the rotation rate was increased. In Fig. 19, these changes on vorticity magnitude over the two zones ( $\omega_{Fin} = \omega_{lateral} / \omega_{over}$ , where  $\omega_{over}$  is over fin vorticity and  $\omega_{lateral}$  is lateral wall fin vorticity) were analyzed for case 2 and case 4.

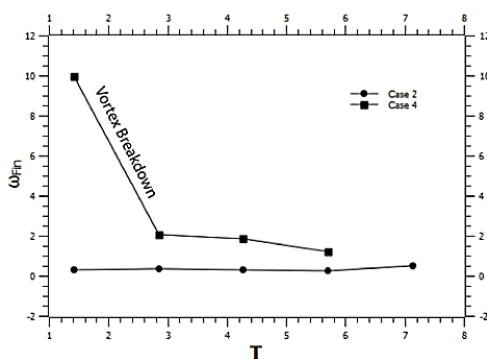


**Fig. 19. Case 2 and case 4,  $1.42 \leq T \leq 14.18$ .**

For case 2, the intensity over the fins prevailed on the flow motion and remained a slight increasing behavior. For this case, no changes in the vortex pattern appeared for a wider rotation rate. On the other hand, the influence of the vorticity generated over the fins showed a decrease of 383% when the rotating rate increased from  $T=1.42$  to  $T=2.85$  for case 4, this decrease was generated because of the vortex's breakdown, which was mainly caused by the appearance of smaller vortices over the fins and the independent rotation of these secondary vortices.

This work proposes the use of a finned Taylor-Couette system as a special reactor which contains vortex sub-reactor which can be controlled in size, shape and position. Additionally, these results have relevance on rotordynamics in order to reduce friction and wasting shaft and rotational mechanics parts (Childs, 2011).

#### 4. CONCLUSIONS

The present study provided a description of the finned Taylor-Couette flow. Specifically, this work focused on an annular flow disturbed by the introduction of different finned rotors. To describe the changes provoked by the introduction of the annular fins, this work described and analyzed the influence of a progressive increment of fin height. The finned vortex flow behavior was compared to the uniform and squared structures that appear on an unfinned system. The comparison between a smooth and finned Taylor-Couette system was performed by using three techniques; which support and complement results with each other. For the first finding, a decrease in the critical Taylor number was identified, and as the fin height increased, the rotation rate required to create the Taylor vortex pattern was less than the previous one.

The classic smooth Taylor-Couette system was analyzed and the appearance of squared and regular toroidal structures was confirmed by the three techniques. However, these structures were disturbed, modifying the shape, size, and position of the vortices by the fin innovation. Each of the finned cases presented different flow behaviors and patterns. The size of the vortex and the vortex wavelength increased up to 50% ( $\lambda' > 1$ ) for smaller values of fin height ( $b' < 0.5$ ), but no vortex breakdown appeared and the flow remained without changes for the wider Taylor range. A lower fin height provokes greater vortex deformations, which tend to extend themselves over the fins, bursting the squared shape. In addition, for the same values of fin height, a decrease in the vorticity magnitude was found, which is due to the deformation, size increment, and extension of the vortex.

On the other hand, the vortex became regular and squared again when there were greater values for fin height ( $b' \geq 0.5$ ), but unlike for a lower fin height, this induced a decrease in wavelength ( $\lambda' < 1$ ). For greater values of fin height, the main vortices tended to be confined by the fins, and both vorticity

magnitude and radial flow rate increased because of the radial velocity magnitude rising. Additionally, the vortex breakdown provoke the development of secondary smaller vortices, the vortex features of this secondary vortices depend on rotating conditions and the relationship between the gap over fins and the fin height.

The proposed finned system can provide a high level of control over the size, position, and vortex number, which could be an advantage in chemical and medical analysis. These same results must to be apply to rotor-dynamic field.

#### ACKNOWLEDGMENTS

The authors appreciate the financial support provided by CONACYT, and by the Instituto de Ingeniería de the Universidad Nacional Autónoma de México.

#### REFERENCES

- Abcha, N., N. Latrache, F. Dumunchel and I. Mutabazi (2008). Qualitative relation between reflective light intensity by Kalliroscope flakes and velocity field in the Taylor-Couette system. *Experiments in fluids* 45:85-94.
- Braun, W., F. De Lillo and B. Eckhardt (2006). Geometry of particle paths in turbulent flows. *Journal of turbulence* 7, 62.
- Childs, P. (2011). Rotating flow. *Elsevier* 185.
- Chong, M.S., A. E. Perry and B. J. Cantwell (1990). A general classification of three-dimensional flow fields. *Physics of Fluids*, A 2, 765-777.
- Deng, R., D. Arifin, M. Chyn and C. Wang (2010). Taylor vortex flow in presence of internal baffles. *Chemical Engineering Science* 65, 4598-4605.
- Dominguez-Lerma, M. A., Guenter Ahlers and David S. Cannell (1984). Effects of Kalliroscope flow visualization particles on rotating Couette-Taylor flow, *Physics of fluids*, 28, 1204.
- Ikedda, E. and T. Maxworthy. (1994). Spatially forced corotating Taylor-Couette flow. *The American physical Society*, 49 6.
- Jeng, T., S. Tzeng and C. Lin (2006). Heat transfer enhancement of Taylor-Couette-Poiseuille flow in an annulus by mounting longitudinal ribs on the rotating inner cylinder. *International Journal of heat and mass transfer* 50, 381-390.
- Koschmieder, E. L. (1975). Effect of finite disturbances on axisymmetric Taylor vortex flow, *The physics of fluids*, 18, 5.
- Laguerre, R., C. Nore, J. Leorat and J. L. Guermond (2008). Cyclic nonlinear dynamo action in a finite Taylor Couette flow. *Journal of Physics* 137, 1.
- Liu, D., I. Kang, J. Cha and H. Kim (2011). Experimental study on radial temperature gradient effect of a Taylor-Couette flow with axial wall slits. *Experimental Thermal and Fluid science* 35, 1282-1292.
- Mahlout, M., A. Mahamdia and M. Kristiawan (2015). Experimental investigations of the spherical Taylor-Couette flow. *Journal of Applied Fluid Mechanics* 9, 131-137.
- Manela, A. and I. Frankel (2007). On the compressible Taylor-Couette problem. *Journal of Fluid Mechanics* 588, 59-64
- Matisse, P. and M. Gorman (1984). Neutrally buoyant anisotropic particles for flow visualization. *Physics of Fluids* 27, 759-760.
- Ogihara, T. and M. Nomura (2002). Continuous Synthesis of Monodispersed Alumina Particles by the Hydrolysis of Metal Alkoxide Using Taylor Vortex. *KONA powder and particle journal* 20 231-232.
- Patankar, S. (1980). *Numerical heat transfer and fluid flow*, Series in computational methods in mechanics and thermal sciences, Taylor and Francis.
- Pawar, S. and B.N. Thorat (2012). CFD simulation of Taylor-Couette flow in scraped surface heat exchanger, 2012. *Chemical Engineering Research and Design* 90, 313-322.
- Peng, J. and K. Zhu (2010). Linear instability of two-fluid Taylor-Couette flow in the presence of surfactant. *Journal of Fluid Mechanics* 651, 357-361
- Richter, O., H. Hoffmann and B. Kraushaar-Czarnetzki (2008). Effect of the rotor shape on the mixing characteristics of a continuous flow Taylor-vortex reactor. *Chemical Engineering Science* 63 3504-3513.
- Richter, O., M. Menges and B. Kraushaar-Czarnetzki (2009). Investigation of mixing in a rotor shape modified Taylor-vortex reactor by the means of a chemical test reaction. *Chemical Engineering Science* 64, 2384-2386.
- Rüdiger, G., M. Gellert, M. Schultz and R. Hollerbach (2010). Dissipative Taylor-Couette flows under the influence of helical magnetic fields. *Physical review E* 82, 0163119, 1-3.
- Sang-Hyuk, L., C. Hee-Taeg, P. Cheol-Woo and K. Hyoung-Bum (2009). Experimental investigation of the effect of axial wall slits on Taylor-Couette flow. *Fluid Dynamics Research* 41, 045502 12
- Singh, J. and R. Bajaj (2005). Couette flow in ferrofluids with magnetic field. *Journal of Magnetism and Magnetic Materials* 294, 53-55.
- Sprague, M., Weidman P., Macumber S. and Fischer P. (2008), Tailored Taylor Vortices, *Physics of fluids*, 20 014102-1.

M. Carlos Álvarez *et al.* / *JAFM*, Vol. 12, No. 5, pp. 1371-1382, 2019.

Sprague, M. and Weidman P. (2009), Continuously tailored Taylor Vortices, *Physics of fluids*, 21 114106.

Taylor, G. (1923). Stability of a Viscous Liquid Contained between Two Rotating Cylinders.

*Mathematical, Physical & Engineering Sciences* 223, 289-294.

White, F. (1999). Fluids mechanics. *Mc Graw Hill*.